FAST ANALYSIS OF ELECTROMAGNETIC TRANSMISSION THROUGH ARBITRARILY SHAPED AIRBORNE RADOMES USING PRECORRECTED-FFT METHOD

X.-C. Nie and N. Yuan

Temasek Laboratories
National University of Singapore
5 Sports Drive 2, Singapore 117508

L.-W. Li and T.-S. Yeo

Department of Electrical and Computer Engineering
National University of Singapore
10 Kent Ridge Crescent, Singapore 119260

Y.-B. Gan

Temasek Laboratories
National University of Singapore
5 Sports Drive 2, Singapore 117508

Abstract—A fast technique based on the Poggio, Miller, Chang, Harrington and Wu (PMCHW) formulation and the precorrected-FFT method is presented for accurate and efficient analysis of electromagnetic transmission through dielectric radomes of arbitrary shape (including airborne radomes). The method of moments is applied to solve the integral equations in which the surfaces of the radomes are modeled using surface triangular patches and the integral equations are converted into a linear system in terms of the equivalent electric and magnetic surface currents. Next, the precorrected-FFT method, a fast approach associated with $O(N^{1.5} \log N)$ or less complexity, is used to eliminate the requirement of generating and storing the square impedance matrix and to speed up the matrix-vector product in each iteration of the iterative solution. Numerical results are presented to validate the implementation and illustrate the accuracy of the method.

1. INTRODUCTION

Layered dielectric radomes are often used to house airborne scanning radar antennas to protect the antennas from a variety of environmental and aerodynamical effects. However, the presence of radome will affect the radiation performance of the enclosed antennas significantly due to interactions of the antenna fields with the radome. A careful analysis of the antenna-radome system is thus necessary in order to investigate what the effects of a dielectric radome are and how the effects can be minimized. So far, a variety of different approaches have been employed to investigate the modification of the radiation pattern of an antenna covered by a radome. These approaches can be divided into three categories: 1) high-frequency (HF) methods such as the ray-tracing technique [1–3]; the plane wave spectrum-surface integral technique [4], the physical optics method (PO) and dielectric physical optics (DPO) technique [5]; 2) low-frequency (LF) methods such as the method of moments (MoM) [6, 7]; the finite element method (FEM) [8], and the method of regularization (MOR) [9]; and 3) analytical methods such as the dyadic Greens function method and iterative interaction procedure [10, 11] which provide more physical insight but are applicable to radomes of special shapes.

    An important assumption of high frequency methods is that the structures have smooth surfaces and electrically large radii of curvature. For most realistic airborne radomes, this assumption is valid. For some types of radomes that have sharp tips such as the ogive or cone, however, HF approaches cannot be employed since the locally flat surface assumption is not valid in that region. On the other hand, low frequency (LF) methods, although providing accurate solution to the problem as compared to the HF solution, are associated with extensive computational requirements. To deal with this problem, one way is to use a hybrid method that combines the LF method to model

the tip region of the dielectric radome and the HF method to treat the flat smooth section of the radome, as in [12]. Another way is to use fast algorithms to reduce the memory requirement and computational complexity of the LF methods. For instance, in [13] and [14], the multilevel fast multiple algorithm (MLFMA) and the conjugate gradient fast Fourier transform (CG-FFT) method were, respectively, used to solve the volumetric integral equations (VIE) associated with antenna-radome interaction problems. In this paper, we present an alternative method which belongs to the latter type. In the approach, the problem is formulated by a set of coupled integral equations in terms of the equivalent surface electric and magnetic currents. The method of moments (MoM) is applied to solve the integral equations. The surfaces of the radome are approximated by planar triangular patches and the Rao-Wilton-Glisson (RWG) functions [15] are used for both expansion and testing functions. Next, the resultant numerical system is solved iteratively and the precorrected-FFT (P-FFT) method is employed to expedite the solution procedure and reduce the memory requirement. The resultant method can be applied to efficiently and accurately analyze dielectric radomes of sizes much larger than that can be analyzed by the conventional MoM. It is evident that it provides higher accuracy than high frequency methods.

In the following section, the surface integral equation formulation for a layered dielectric radome of arbitrary shape is first presented. Next, the method of moments solution and the precorrect-FFT approach are discussed in detail. In Section 3, some numerical examples are presented to illustrate the accuracy and capability of the method. Spherical and Von Karman radomes of different size are studied and both the field inside the radome under a plane wave incidence (the "receiving mode") and the radiated far field due to an elementary dipole inside the radome (the "transmitting mode") are computed. The computed results are in excellent agreement with the available published data, which demonstrates the applicability and accuracy of the method.

2. FORMULATION

2.1. Surface Integral Equation Formulation

Consider a dielectric radome of arbitrary shape residing in a homogenous background medium with parameters (ε_0, μ_0), as shown in Fig. 1. The outer surface of the radome is denoted by S_0 and the inner surface is denoted by S_1. The radome has a permittivity ε_1 and a permeability of μ_1. The radome can be excited by two impressed sources: the incidence plane wave from outside (the receiving-mode
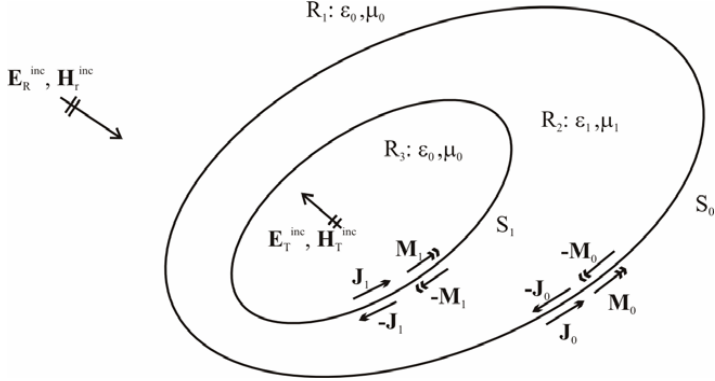
Figure 1. Geometry of an arbitrary shaped radome excited by two sets of impressed sources.

source) and the radiation field of a dipole inside the radome (the transmitting-mode source). Let $(\mathbf{E}_R^{inc}, \mathbf{H}_R^{inc})$ and $(\mathbf{E}_T^{inc}, \mathbf{H}_R^{inc})$ denote the incident fields produced by the receiving-mode source and the transmitting-mode source respectively. It is noted that the incident field is defined as the field that exists in the absence of the radome.

By invoking the equivalence principle, three equivalent problems are formulated, valid for the region external to the surface S_0 (Region 1), bounded by S_0 and S_1 (Region 2), and internal to S_1 (Region 3), respectively. By introducing equivalent electric and magnetic currents $(\mathbf{J}_0, \mathbf{M}_0)$, $(-\mathbf{J}_0, -\mathbf{M}_0)$, and $(\mathbf{J}_1, \mathbf{M}_1)$, $(-\mathbf{J}_1, -\mathbf{M}_1)$ on opposite sides of the surfaces S_0 and S_1 respectively, and enforcing the boundary conditions on the electric and magnetic fields across the interfaces, the following coupled field integral equations are obtained in terms of the unknown

$$[\mathbf{E}_0(\mathbf{J}_0)+\mathbf{E}_1(\mathbf{J}_0)+\mathbf{E}_1(\mathbf{J}_1)+\mathbf{E}_0(\mathbf{M}_0)+\mathbf{E}_1(\mathbf{M}_0)+\mathbf{E}_1(\mathbf{M}_1)]\Big|_{\tan}$$

$$= -\mathbf{E}_R^{inc}\Big|_{\tan} \qquad \text{on} \qquad S_0, \tag{1a}$$

$$[\mathbf{E}_1(\mathbf{J}_0)+\mathbf{E}_0(\mathbf{J}_1)+\mathbf{E}_1(\mathbf{J}_1)+\mathbf{E}_1(\mathbf{M}_0)+\mathbf{E}_0(\mathbf{M}_1)+\mathbf{E}_1(\mathbf{M}_1)]\Big|_{\tan}$$

$$= -\mathbf{E}_T^{inc}\Big|_{\tan} \qquad \text{on} \qquad S_1, \tag{1b}$$

$$[\mathbf{H}_0(\mathbf{J}_0)+\mathbf{H}_1(\mathbf{J}_0)+\mathbf{H}_1(\mathbf{J}_1)+\mathbf{H}_0(\mathbf{M}_0)+\mathbf{H}_1(\mathbf{M}_0)+\mathbf{H}_1(\mathbf{M}_1)]\Big|_{\tan}$$

$$= -\mathbf{H}_R^{inc}\Big|_{\tan} \qquad \text{on} \qquad S_0, \tag{1c}$$

$$\left[\mathbf{H}_1(\mathbf{J}_0) + \mathbf{H}_0(\mathbf{J}_1) + \mathbf{H}_1(\mathbf{J}_1) + \mathbf{H}_1(\mathbf{M}_0) + \mathbf{H}_0(\mathbf{M}_1) + \mathbf{H}_1(\mathbf{M}_1)\right]\Big|_{\tan}$$

$$= -\mathbf{H}_T^{inc}\Big|_{\tan} \qquad \text{on} \qquad S_1, \tag{1d}$$

where $\mathbf{E}_i(\mathbf{J}_j)$ and $\mathbf{H}_i(\mathbf{J}_j)$, $(i = 0, 1$ and $j = 0, 1)$ represent the electric and magnetic fields produced by the electric currents $\mathbf{J}_j$ in the homogenous media i respectively. $\mathbf{E}_i(\mathbf{M}_j)$, $\mathbf{H}_i(\mathbf{M}_j)$ represent the fields produced by the magnetic current $\mathbf{M}_j$ in the homogenous medium i. The subscript 'tan' denotes the tangential components. Eq. (1) is known as the PMCHW formulation for dielectric objects [15], which is found to be free of interior resonances and yield accurate and stable solutions. The fields in Eq. (1) can be computed from the surface current by

$$\mathbf{E}_i(\mathbf{J}_j) = -j\omega\mathbf{A}_{ij} - \nabla\mathbf{\Phi}_{ij} \tag{2a}$$

$$\mathbf{E}_i(\mathbf{M}_j) = -\frac{\nabla \times \mathbf{F}_{ij}}{\varepsilon_i} \tag{2b}$$

$$\mathbf{H}_i(\mathbf{J}_j) = \frac{\nabla \times \mathbf{A}_{ij}}{\mu_i} \tag{2c}$$

$$\mathbf{H}_i(\mathbf{M}_j) = -j\omega\mathbf{F}_{ij} - \nabla\mathbf{\Psi}_{ij} \tag{2d}$$

where the various vector potentials $\mathbf{A}_{ij}(\mathbf{r})$ and $\mathbf{F}_{ij}(\mathbf{r})$ and the scalar potentials $\mathbf{\Phi}_{ij}(\mathbf{r})$ and $\mathbf{\Psi}_{ij}(\mathbf{r})$ are given by

$$\mathbf{A}_{ij}(\mathbf{r}) = \frac{\mu_i}{4\pi} \int_{S_j} \mathbf{J}_j(\mathbf{r}')G_i(\mathbf{r}, \mathbf{r}')d\mathbf{S}(\mathbf{r}') \tag{3a}$$

$$\mathbf{F}_{ij}(\mathbf{r}) = \frac{\varepsilon_i}{4\pi} \int_{S_j} \mathbf{M}_j(\mathbf{r}')G_i(\mathbf{r}, \mathbf{r}')d\mathbf{S}(\mathbf{r}') \tag{3b}$$

$$\mathbf{\Phi}_{ij}(\mathbf{r}) = -\frac{1}{4\pi j\omega\varepsilon_i} \int_{S_j} \nabla_S' \cdot \mathbf{J}_j(\mathbf{r}')G_i(\mathbf{r}, \mathbf{r}')d\mathbf{S}(\mathbf{r}') \tag{3c}$$

$$\mathbf{\Psi}_{ij}(\mathbf{r}) = -\frac{1}{4\pi j\omega\mu_i} \int_{S_j} \nabla_S' \cdot \mathbf{M}_j(\mathbf{r}')G_i(\mathbf{r}, \mathbf{r}')d\mathbf{S}(\mathbf{r}') \tag{3d}$$

with $G_i(\mathbf{r}, \mathbf{r}')$ is the Green's function defined by

$$G_i(\mathbf{r}) = \frac{e^{-jk_i|\mathbf{r}-\mathbf{r}'|}}{|\mathbf{r} - \mathbf{r}'|} \tag{4}$$

and k_i being the propagation constant in medium i. In the above expressions and subsequent formulations, the time dependence of $e^{j\omega t}$ is assumed and suppressed.

2.2. Method of Moments Solution

For numerical solution of Eq. (1), the dielectric surfaces S_0 and S_1 are discretized into small triangular patches and the equivalent electric and magnetic currents $\mathbf{J}_i, \mathbf{M}_i (i = 0, 1)$ are expanded using the RWG basis functions [15]:

$$\mathbf{J}_i(\mathbf{r}') = \sum_{n=1}^{N_{is}} I_{in} \mathbf{f}_{in}(\mathbf{r}') \tag{5a}$$

$$\mathbf{M}_i(\mathbf{r}') = \eta_0 \sum_{n=1}^{N_{is}} M_{in} \mathbf{f}_{in}(\mathbf{r}') \tag{5b}$$

where I_{in} and M_{in} are the unknown expansion coefficients, N_{is} denotes the number of edges on the surface S_i of the triangulated model, $\mathbf{f}_{in}(\mathbf{r}')$ is the nth RWG basis function associated with the nth edge on S_i and η_0 is the characteristic impedance in free space. The factor of η_0 is required since the H-field equation is normalized by η_0. Substituting (5) into (1) and testing (1a), (1b) with $\mathbf{f}_m$ and (1c), (1d) with $\eta_0 \mathbf{f}_m$ result in a $N \times N$ ($N = 2(N_{0s} + N_{1s})$) matrix equation of the form

$$\mathbf{ZI} = \mathbf{V}. \tag{6}$$

The matrices $\mathbf{Z}$, $\mathbf{I}$ and $\mathbf{V}$ can be written in the following partitioned form

$$\mathbf{Z} = \begin{bmatrix} [Z_{mn}^{J_0 J_0}] & [Z_{mn}^{J_0 J_1}] & [T_{mn}^{J_0 M_0}] & [T_{mn}^{J_0 M_1}] \\ [Z_{mn}^{J_1 J_0}] & [Z_{mn}^{J_1 J_1}] & [T_{mn}^{J_1 M_0}] & [T_{mn}^{J_1 M_1}] \\ [T_{mn}^{M_0 J_0}] & [T_{mn}^{M_0 J_1}] & [Y_{mn}^{M_0 M_0}] & [Y_{mn}^{M_0 M_1}] \\ [T_{mn}^{M_1 J_0}] & [T_{mn}^{M_1 J_1}] & [Y_{mn}^{M_1 M_0}] & [Y_{mn}^{M_1 M_1}] \end{bmatrix} \tag{7a}$$

$$\mathbf{I} = [[I_{0n}] \quad [I_{1n}] \quad [M_{0n}] \quad [M_{1n}]]^T \tag{7b}$$

$$\mathbf{V} = [[V_{0m}] \quad [V_{1m}] \quad [H_{0m}] \quad [H_{1m}]]^T \tag{7c}$$

where "T" denotes the transpose of matrix. Elements of the subvectors $[V_{0m}]$ and $[H_{0m}]$ are given by

$$V_{0m} = -\int_{T_{0m}} \mathbf{f}_{0m}(\mathbf{r}) \cdot \mathbf{E}_R^{inc}(\mathbf{r}) d\mathbf{r} \tag{8a}$$

$$H_{0m} = -\int_{T_{0m}} \mathbf{f}_{0m}(\mathbf{r}) \cdot \eta_0 \mathbf{H}_R^{inc}(\mathbf{r}) d\mathbf{r}. \tag{8b}$$

Similar expressions can be found for elements of $[V_{1m}]$ and $[H_{1m}]$

by replacing the subscript 0 by 1 and the incident fields $\mathbf{E}_R^{inc}(\mathbf{r})$ and $\mathbf{H}_R^{inc}(\mathbf{r})$ by $\mathbf{E}_T^{inc}(\mathbf{r})$ and $\mathbf{H}_T^{inc}(\mathbf{r})$, respectively. Elements of the submatrices of the square moment matrix $\mathbf{Z}$ can be readily obtained from Eq. (1) and the definitions in formulas in (2) and (3). For clarity of the description, we provide the following expressions for some of the submatrices:

$$
\begin{aligned}
Z_{mn}^{J_0 J_0} &= -j\omega \int_{T_{0m}} \mathbf{f}_{0m}(\mathbf{r}) \cdot [\mathbf{A}_{0mn} + \mathbf{A}_{1mn}] \, d\mathbf{r} \\
&\quad + \int_{T_{0m}} \nabla_s \cdot \mathbf{f}_{0m}(\mathbf{r}) \, [\mathbf{\Phi}_{0mn} + \mathbf{\Phi}_{1mn}] \, d\mathbf{r} \tag{9a}
\end{aligned}
$$

$$
T_{mn}^{J_0 M_0} = -\int_{T_{0m}} \eta_0 \mathbf{f}_{0m}(\mathbf{r}) \cdot \nabla \times \left[\frac{\mathbf{F}_{0mn}}{\varepsilon_0} + \frac{\mathbf{F}_{1mn}}{\varepsilon_1} \right] d\mathbf{r} \tag{9b}
$$

$$
T_{mn}^{M_0 J_0} = \int_{T_{0m}} \eta_0 \mathbf{f}_{0m}(\mathbf{r}) \cdot \nabla \times \left[\frac{\mathbf{A}_{0mn}}{\mu_0} + \frac{\mathbf{A}_{1mn}}{\mu_1} \right] d\mathbf{r} \tag{9c}
$$

$$
\begin{aligned}
Y_{mn}^{M_0 M_0} &= -j\omega \int_{T_{0m}} \mathbf{f}_{0m}(\mathbf{r}) \cdot \eta_0^2 \, [\mathbf{F}_{0mn}(\mathbf{r}) + \mathbf{F}_{1mn}(\mathbf{r})] \, d\mathbf{r} \\
&\quad + \int_{T_{0m}} \nabla_s \cdot \mathbf{f}_{0m}(\mathbf{r}) \cdot \eta_0^2 \, [\mathbf{\Psi}_{0mn}(\mathbf{r}) + \mathbf{\Psi}_{1mn}(\mathbf{r})] \, d\mathbf{r}. \tag{9d}
\end{aligned}
$$

Expressions for other submatrices can be written in a similar form but are omitted here. In (9), the vector and scalar potential integrals take the following form, for $i = 0, 1$:

$$
\mathbf{A}_{imn}(\mathbf{r}) = \frac{\mu_i}{4\pi} \int_{T_n} \mathbf{f}_n(\mathbf{r}') G_i(\mathbf{r}, \mathbf{r}') d\mathbf{r}' \tag{10a}
$$

$$
\mathbf{\Phi}_{imn}(\mathbf{r}) = -\frac{1}{4\pi j\omega\varepsilon_i} \int_{T_n} \nabla_s' \cdot \mathbf{f}_n(\mathbf{r}') G_i(\mathbf{r}, \mathbf{r}') d\mathbf{r}' \tag{10b}
$$

$$
\mathbf{F}_{imn}(\mathbf{r}) = \frac{\varepsilon_i}{4\pi} \int_{T_n} \mathbf{f}_n(\mathbf{r}') G_i(\mathbf{r}, \mathbf{r}') d\mathbf{r}' \tag{10c}
$$

$$
\mathbf{\Psi}_{imn}(\mathbf{r}) = -\frac{1}{4\pi j\omega\mu_i} \int_{T_n} \nabla_s' \cdot \mathbf{f}_n(\mathbf{r}') G_i(\mathbf{r}, \mathbf{r}') d\mathbf{r}'. \tag{10d}
$$

It is noted that $\mathbf{F}_{imn}$ and $\mathbf{\Psi}_{imn}$ produced by the nth magnetic current expansion function are respectively the dual of $\mathbf{A}_{imn}$ and $\mathbf{\Phi}_{imn}$ produced by the same function with an electric current expansion function. These duality relationships will be used in the following precorrected-FFT approach.

2.3. Precorrected-FFT Method

The data storage requirement of the full matrix generated by the method of moments is of the order of $O(N^2)$, while the complexity of a direct solution is $O(N^3)$. Therefore, we are interested in developing a fast algorithm with lower order of complexity and storage requirements. The precorrected-FFT (P-FFT) method is a fast method associated with $O(N^{3/2} \log N)$ or less complexity. It was originally proposed by Philips and White [16, 17] to solve the electrostatic integral equations associated with capacitance extraction problems and was recently extended by the present authors to the analysis of scattering by large conducting objects [18, 19] and microstrip antenna arrays [20]. Like other fast algorithms, the P-FFT method also works on approximating the far-zone interactions. The acceleration of the solution in (6) is accomplished by filling only an order-N subset of $\mathbf{Z}$ and computing the matrix-vector product $\mathbf{ZI}$ in two parts, that is

$$\mathbf{ZI} = \mathbf{Z}_{near}\mathbf{I} + \mathbf{Z}_{far}\mathbf{I}. \tag{11}$$

where $\mathbf{Z}_{near}$ is sparse and contains only the entries associated with elements separated less than a threshold distance, and $\mathbf{Z}_{far}\mathbf{I}$ contains the remaining interactions that will be computed by an approximation technique.

To implement the P-FFT algorithm, the entire object is enclosed in a uniform rectangular grid. The triangular patches are sorted into cells formed by the grid, with each cell containing only a few triangular patches. Then the matrix-vector multiplication can be approximated in a four-step procedure: (1) to project the element source distributions to point sources on the uniform grid, (2) to compute the potentials at the grid points due to the grid sources by FFT-accelerated convolutions, (3) to interpolate the grid-point potentials onto the elements, and (4) to add the precorrected direct nearby interactions.

First, we need to construct the projection operators that can replace the set of element source distributions in the cell with an equivalent set of point sources on the grid. As noted before, the only difference between $\mathbf{F}_{imn}$ and $\mathbf{A}_{imn}$, $\mathbf{\Psi}_{imn}$ and $\mathbf{\Phi}_{imn}$ is a constant due to the use of the same expansion functions for the electric and magnetic currents. Therefore, although both electric and magnetic currents exist in the problem, we need only to construct the projection operators for one current, for example, the electric current. Without loss of generality, the projection of the magnetic currents can then be performed using the same projection operators.

Assume that the nth RWG basis function is contained in a given cell k. The current and charge (either electric or magnetic)

distributions on the two nth RWG patches are then projected onto the grids surrounding the nth edge. Point sources on the grids can be set at the cell vertices (grid-order $p = 2$), or at half the spacing of the vertices (grid-order of $p = 3$), etc., as desired for accuracy. Select N_c test points on the surface of a sphere of radius r_c whose center is coincident with the center of the cell k. The radius r_c can be arbitrarily selected as long as all the cell vertices are entirely enclosed in the sphere. Enforcing the vector potential produced by the electric currents at the p^3 grid points to match that produced by the original electric current distributions on the triangular patches at the test points, we obtain

$$\mathbf{A}_{i,q}^{pt} = \tilde{\mathbf{A}}_{i,q}^{gt}, \qquad q = 1, 2, \cdots N_c, \qquad i = 0, 1 \tag{12}$$

where $\mathbf{A}_{i,q}^{pt}$ and $\tilde{\mathbf{A}}_{i,q}^{gt}$ denote the vector potentials at the qth test point due to the original patch currents and the grid currents respectively, whose expressions are given by

$$\mathbf{A}_{i,q}^{pt}(\mathbf{r}_q^t) = \frac{\mu_i}{4\pi} \int_S I_n \mathbf{f}_n(\mathbf{r}') \frac{e^{-jk_i|\mathbf{r}_q^t - \mathbf{r}'|}}{|\mathbf{r}_q^t - \mathbf{r}'|} dS' \tag{13a}$$

$$\tilde{\mathbf{A}}_{i,q}^{gt}(\mathbf{r}_q^t) = \frac{\mu_i}{4\pi} \sum_{l=1}^{p^3} \left(\hat{J}_{x,l}\hat{\mathbf{x}} + \hat{J}_{y,l}\hat{\mathbf{y}} + \hat{J}_{z,l}\hat{\mathbf{z}} \right) \frac{e^{-jk_i|\mathbf{r}_q^t - \mathbf{r}_l|}}{|\mathbf{r}_q^t - \mathbf{r}_l|} \tag{13b}$$

with $\mathbf{r}_q^t$ and $\mathbf{r}_l$ being the position vectors at the qth test point and the lth grid point, respectively, and $\hat{J}_{x,l}$, $\hat{J}_{y,l}$, $\hat{J}_{z,l}$ being the three components of the current at the lth grid point. The subscript i represents the medium in which the vector potentials are computed. Substituting (13) into (12), and decomposing the patch currents into three components yield

$$\mathbf{P}_{i,u}^{gt} \hat{J}_{i,u} = \mathbf{P}_{i,u}^{pt} I_n, \qquad u = x, y, z \tag{14}$$

where $\hat{J}_{i,u} \in R^{p^3 \times 1}$ denote the vectors consisting of the u components of the currents at the grid point $\mathbf{P}_{i,u}^{gt} \in R^{N_c \times p^3}$ represent the mappings between the grid currents and the test-point potentials given by

$$\mathbf{P}_{i,u}^{gt}(q, l) = \frac{\mu_i}{4\pi} \frac{e^{-jk_i|\mathbf{r}_q^t - \mathbf{r}_l|}}{|\mathbf{r}_q^t - \mathbf{r}_l|}. \tag{15}$$

By construction, the relative positions of the grid points and the test points are identical for each cell, and therefore $\mathbf{P}_{i,u}^{gt}$ are the same for each cell. The component, $\mathbf{P}_{i,u}^{pt} \in R^{N_c \times N(k)}$, represent the mappings

between the patch currents and the test-point potentials, $N(k)$ is the number of the basis functions contained in cell k. $\mathbf{P}_{i,u}^{pt}$ can be written as

$$\mathbf{P}_{i,u}^{pt}(q,n) = \frac{\mu_i}{4\pi} \int_S \mathbf{f}_n(\mathbf{r}') \cdot \hat{\mathbf{u}} \frac{e^{-jk_i|\mathbf{r}_q^t - \mathbf{r}'|}}{|\mathbf{r}_q^t - \mathbf{r}'|} dS'. \tag{16}$$

Since the collocation Equation (14) is linear in the patch and grid current distributions, the contribution of the nth basis function in cell k to $\hat{J}_{i,u}$ can be represented by three column vectors $W_{i,u}(k,n)$, given by

$$W_{i,u}(k,n) = [\mathbf{P}_{i,u}^{gt}]^+ \mathbf{P}_{i,u}^{pt,n} \tag{17}$$

where $\mathbf{P}_{i,u}^{pt,n}$ denotes the nth column of $\mathbf{P}_{i,u}^{pt}$ and $[\mathbf{P}_{i,u}^{gt}]^+$ indicates the generalized inverse of $\mathbf{P}_{i,u}^{gt}$. $W_{i,u}(k,n)$, identifies the current projection operator computed in medium i. For any basis function n in cell k, this projection operator generates a subset of the grid currents $\hat{J}_{i,u}$. The contribution to $\hat{J}_{i,u}$ from the currents in cell k can be computed by summing over all the currents in this cell, i.e.,

$$\hat{J}_{i,u} = \sum_n \mathbf{W}_{i,u}(k,n) I_n \tag{18}$$

Patch currents outside cell k may contribute to some of the elements of $\hat{J}_{i,u}$ in the case of shared grids. Following the above procedure, we can project the patch current $I_n\mathbf{f}_n$ onto the p^3 grid points surrounding cell k.

The above formulae are applicable to the projection of the patch current. Similarly, by matching the scalar potential due to the p^3 grid charges and that due to the actual patch charge distribution at the test points, we can construct the charge projection operator $W_{i,c}(k,n)$. The accuracy of the above projection scheme depends on the proper selection of the test points $\mathbf{r}^t$. The criteria for the choice of the test points can be found in [21, 22]. Note that since the Green's functions changed due to the constitutive properties for different media, the projections are performed for each medium separately, namely, when the vector or scalar potentials in medium i are to be computed, the projection operators corresponding to medium i are used for the projection. For a multilayer dielectric object such as the dielectric radomes, the present projection method does not require extra FFTs in the computation of the grid potentials, as compared with the AIM which employs a Green's function independent projection operator

[23]. On the contrary, the present projection method yields a much more accurate projection since it fully explores the information of the Green's functions.

Once the patch source distributions have been projected onto uniform grids, the relationship between the vector and scalar potentials at the grid points and the grid sources is in fact a 3-D convolution. The convolutions can be efficiently computed using the fast Fourier transform (FFT) due to the Toeplitz property of the Green's function matrix. Hence, the vector and scalar potentials at the grid points can be computed by

$$
\hat{A}_u \;\; = \;\; DFT^{-1}\left\{DFT\{G\} \cdot DFT\{\hat{J}_u\}\right\}, \qquad u = x, y, z \quad (19\text{a})
$$

$$
\hat{\boldsymbol{\Phi}}_u \;\; = \;\; DFT^{-1}\left\{DFT\{G\} \cdot DFT\{\hat{q}\}\right\} \qquad\qquad\qquad (19\text{b})
$$

where DFT and DFT^{-1} denote the FFT and inverse FFT, respectively. The entries of G are the Green's functions between grid points in the corresponding medium. In practice, each convolution requires one forward and one inverse three-dimensional FFT. The FFT of the kernel matrix G need to be computed only once.

After the grid potentials are computed, the potentials on the triangular patches can be obtained through interpolation. Assume that $[V(k,j)]^T$ denotes the interpolation operator and H denotes the inverse and direct FFT operations in (19). Thus, the projection, followed by convolution and interpolation, gives the grid approximation to the potentials

$$
\mathbf{A}_G \;\; = \;\; V^T H W \mathbf{J} \qquad\qquad\qquad (20\text{a})
$$

$$
\boldsymbol{\Phi}_G \;\; = \;\; V^T H W_c (\nabla \cdot \mathbf{J}). \qquad\qquad (20\text{b})
$$

Both the projection and the interpolation operators are represented by sparse matrices.

The difficulty with the above three steps is that the near-field interactions are poorly approximated in the projection/interpolation. A more accurate calculation of the interactions between nearby patches is needed and the inaccurate contribution from the use of the grid also need to be removed. This process is referred to as "pre-correction". Define a "pre-corrected" direct interaction operator

$$
\tilde{P}(k,l) = P(k,l) - V(k)^T H(k,l) W(l). \qquad\qquad (21)
$$

The exact vector potential $\mathbf{A}(k)$ and scalar potential $\boldsymbol{\Phi}(k)$ for each cell

k can be obtained by

$$\mathbf{A}(k) = \mathbf{A}_G(k) + \sum_{l \in M(k)} \tilde{P}(k,l)\mathbf{J}_l, \qquad (22a)$$

$$\mathbf{\Phi}(k) = \mathbf{\Phi}_G(k) + \sum_{l \in M(k)} \tilde{P}(k,l)(\nabla \cdot \mathbf{J}_l) \qquad (22b)$$

where $M(k)$ denotes the indices of the set of cells which are "close to" cell k. Since for each k, $M(k)$ is a small set and each matrix $\tilde{P}(k,l)$ is also small, this step is also a sparse operation.

So far, the submatrix-vector products $[Z_{mn}^{J_i J_j}][I_{jn}]$ and $[Y_{mn}^{M_i M_j}]$ $[M_{jn}]$ ($i = 0,1$, $j = 0,1$) can be readily obtained, as the vector and scalar potentials have been efficiently computed using the above precorrected-FFT formulation. However, the evaluation of the products $[T_{mn}^{J_i M_j}][M_{jn}]$ and $[T_{mn}^{M_i J_j}][I_{jn}]$ still need further treatment. In [22] where the AIM was applied to the dielectric scattering problems, the authors evaluated these products by projecting the $\nabla \times \mathbf{f}_n$ operator onto the uniform grid as well as the basis function $\mathbf{f}_n$ and its divergence $\nabla \cdot \mathbf{f}_n$. In this paper, we apply a simplified approach which avoids the projection of the $\nabla \times \mathbf{f}_n$ operator. For example, the elements of $[T_{mn}^{M_0 J_1}][I_{1n}]$ can be written in the following form

$$\begin{aligned} T_{mn}^{M_0 J_1} I_{1n} &= \int_{T_{0m}} \eta_0 \mathbf{f}_{0m}(\mathbf{r}) \cdot \frac{\nabla \times \mathbf{A}_{1mn} I_{1n}}{\mu_1} d\mathbf{r} \\ &= \int_{T_{0m}} \eta_0 \mathbf{f}_{0m}(\mathbf{r}) \cdot \frac{1}{\mu_1} \left\{ \left(\frac{\partial A_{1mn,z} I_{1n}}{\partial y} - \frac{\partial A_{1mn,y} I_{1n}}{\partial z} \right) \hat{\mathbf{x}} \right. \\ &\quad + \left(\frac{\partial A_{1mn,x} I_{1n}}{\partial z} - \frac{\partial A_{1mn,z} I_{1n}}{\partial x} \right) \hat{\mathbf{y}} \\ &\quad \left. + \left(\frac{\partial A_{1mn,y} I_{1n}}{\partial x} - \frac{\partial A_{1mn,x} I_{1n}}{\partial y} \right) \hat{\mathbf{z}} \right\} d\mathbf{r} \qquad (23) \end{aligned}$$

The partial derivatives in (23) can be replaced by the corresponding differences that can be computed through the vector potentials at several points in the vicinity of the observation point. Knowledge of these potentials can be readily obtained through interpolation since the vector potentials at grid points have been computed by the FFTs. This approach only requires several extra interpolations and avoids additional efforts to project the $\nabla \times \mathbf{f}_n$ operator and to perform the corresponding FFTs.
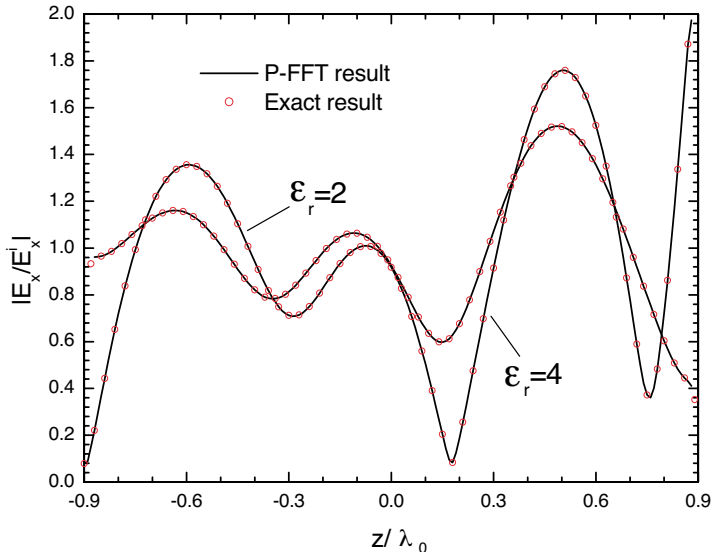
Figure 2. The normalized magnitude of the x-component of the total electric field at various points along the normalized z-axis inside a spherical radome.

3. NUMERICAL RESULTS

The numerical examples given below serve only to validate the implementation and illustrate the accuracy of the method. The actual speed-up achieved by the P-FFT has already been demonstrated in [18] and is beyond the scope of this paper.

The first example is a spherical radome of inner radius $0.9\lambda_0$ and outer radius $1.0\lambda_0$. The radome is centered at the origin and is excited by a x-polarized, $+z$-traveling plane wave (receive mode). The inner and the outer surfaces are approximated by 2108 and 2586 triangular patches respectively, leading to 14082 unknowns. For the P-FFT method, a grid spacing of $0.1\lambda_0$ is used and the grid order is set to be $p = 3$ and the near-field threshold distance to be $0.2\lambda_0$. The normalized magnitude of the x-component of the total electric field at various points along the z-axis inside the radome for two different dielectric constants ($\varepsilon_r = 2$ and $\varepsilon_r = 4$) is shown in Fig. 2. Fig. 3 shows the phase of E_x. It is observed that the computed results agree very well with the exact results [6] for both the magnitude and phase, validating the accuracy of the present method.

The second example is a Von Karman radome (a BOR structure)
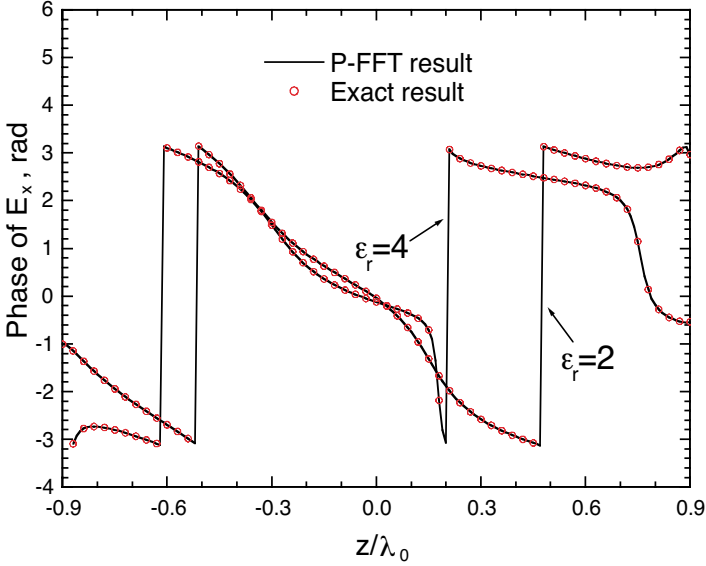
Figure 3. Phase of the x-component of the total electric field.

as shown in Fig. 4(a). The generating curve of the radome is given by

$$r_i = \frac{D_i}{2\sqrt{\pi}} \left\{ \cos^{-1}\left(1 - \frac{2z_i}{L_i}\right) - \frac{1}{2}\sin^{-1}\left[2\cos^{-1}\left(1 - \frac{2z_i}{L_i}\right)\right] \right\}^{\frac{1}{2}}, \ i = 0, 1 \tag{24}$$

with

$$r_i = \sqrt{x_i^2 + y_i^2}. \tag{25}$$

The tip of the ith surface is at $(0, 0, L_i/2)$ and its base is a circle of diameter $L_i/2$ at $z = -L_i/2$. In this example, the lengths of the outer and the inner surfaces L_0 and L_1 are respectively $2.0\lambda_0$ and $1.8\lambda_0$ while the corresponding diameters D_0 and D_1 are λ_0 and $0.9\lambda_0$ respectively. The dielectric constant is 4.0. Each of the surfaces is discretized into 2800 triangles, resulting in a total of 16800 unknowns. Fig. 4(b) shows the magnitude of E_x inside the radome when it is illuminated by a x-polarized plane wave incident along the z axis from the top. The field is computed along the z-axis. Both results obtained by the P-FFT method and the traditional MoM [6] are shown for comparison. Again, good agreement is observed.

Fig. 5 shows the normalized magnitude of E_x at the center of a Von Karman radome illuminated by a θ-polarized plane wave with the incident angle $\phi^i = 0°$ and θ^i varies from $90°$ to $180°$. The size

(a)

(b)
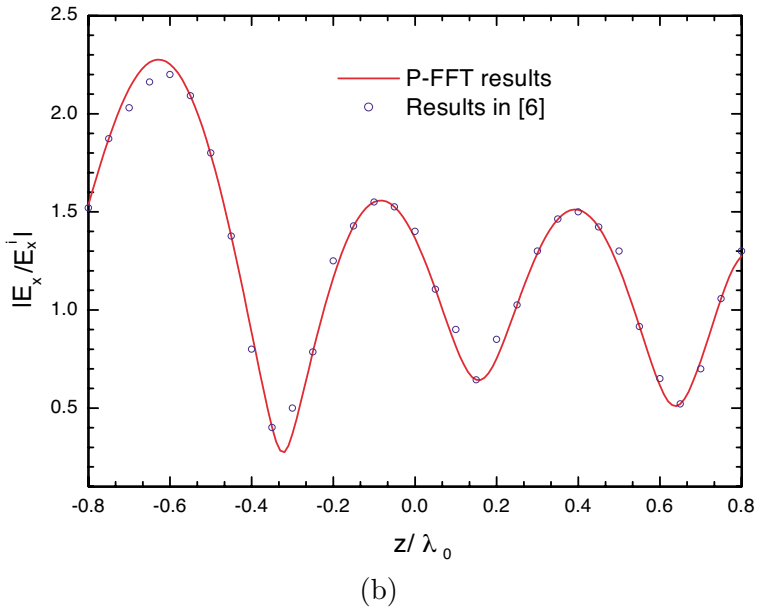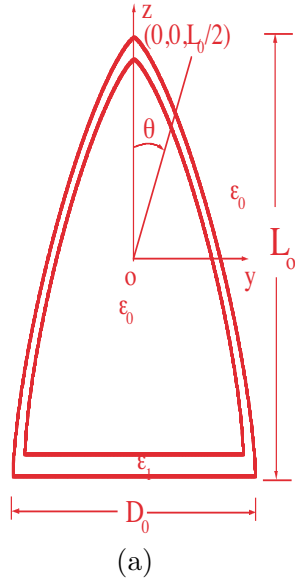
Figure 4. (a) The geometry of a Von Karman radome (b) The normalized magnitude of E_x along the z-axis inside the Von Karman radome.
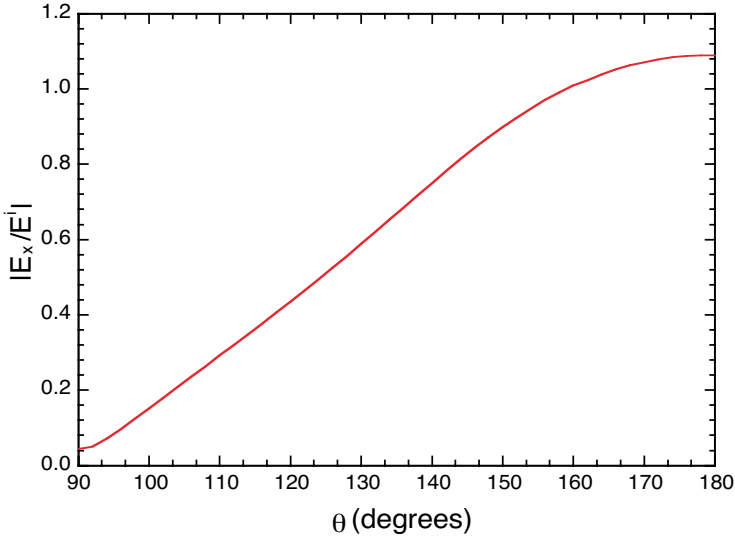
Figure 5. The normalized magnitude of E_x at the center of a Von Karman radome versus the incident angle.

of the radome is the same as in Fig. 5 and the dielectric constant is $\varepsilon_r = 1.75 - j0.3$. It can be seen that when $\theta^i = 180°$, the magnitude of E_x is largest since the incident wave is actually x-polarized in this case. When $\theta^i = 90°$, the incident wave is z-polarized and E_x is the cross-polar field. Therefore, it is smaller than other cases. However, E_x cannot be neglected despite its small value, unlike in free space, where E_x is zero when the incident field is z-polarized. This phenomenon is known as depolarization, one of the important effects caused by the presence of radomes.

In the above examples the radomes are excited in the receive mode. Next, we give some examples for the transmit mode. Fig. 6 shows the far field pattern of the E_θ component transmitted through a spherical radome due to a z-directed electric dipole placed at the center of the radome. Two different sizes (inner radius of $0.5\lambda_0$ and $0.9\lambda_0$) and two different dielectric constants ($\varepsilon_r = 1.0$ and 2.5) are considered. The thickness of the radome wall is $0.1\lambda_0$ in all cases. The magnitude is normalized by the peak value (occurs at $\theta = 90°$) of the far field radiated by the same dipole in free space. It can be seen that the two curves for different sizes coincide with each other when ε_r equals 1.0, since the dielectric media is free space in this case. Besides, when ε_r equals 2.5, the field transmitted through the smaller radome is larger than the field radiated by the dipole in free space whereas
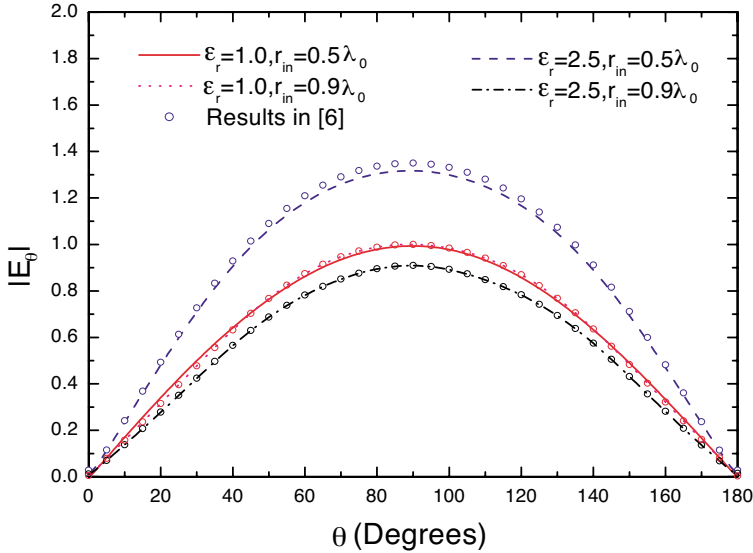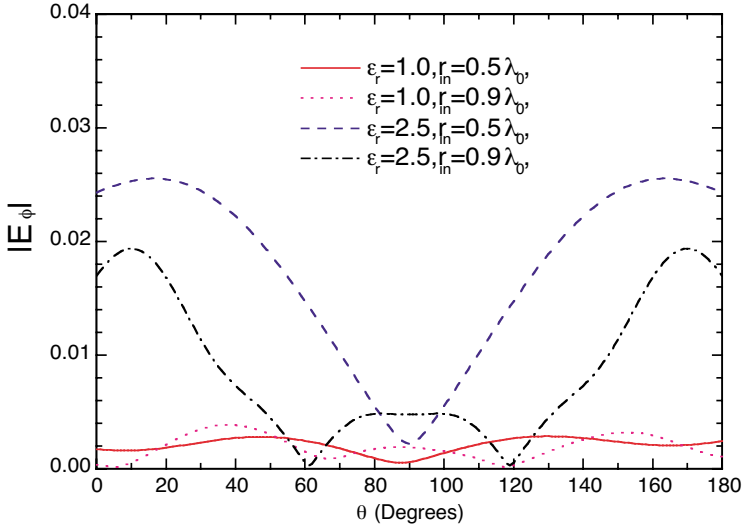
Figure 6. Far field pattern of the field (E_θ) transmitted through a spherical radome.

the field transmitted through the larger radome is smaller than the field radiated by the dipole in free space. This is probably due to the interactions of the radiation field with the radome. The exact results from [6] are also given in the figure by hollow circles.

Fig. 7 shows the far field pattern of the E_ϕ component for the same example. As we know, the z-directed dipole does not radiate ϕ component field in free space. This fact is validated by the computed results since E_ϕ are sufficiently small (less than 0.005) to be negligible when ε_r equals 1.0. However, E_ϕ cannot be ignored when the radome actually exists (ε_r does not equal 1.0) due to the depolarization effect caused by the radome. For example, when ε_r equals 2.5, the peak value of E_ϕ is up to 0.025 and 0.02 respectively for $r_{in} = 0.5\lambda_0$ and $r_{in} = 0.9\lambda_0$. It is also observed that the strongest depolarization occurs in the direction near $\theta = 0°$ and $\theta = 180°$. Further, the larger the radome the weaker is the depolarization effect.

In the last example, we consider a larger spherical dielectric radome with a 9-element uniform dipole array located on the z-axis inside the radome [13]. The inner radius of the radome is $1.2\,m$ and the thickness is $0.08\,m$. The dipole array operates at $300\,MHz$. The inter-element spacing is 0.25λ and the fifth element is located at the center of the shell. The inner surface and the outer surface are

Figure 7. Far field pattern of the field (E_ϕ) transmitted through a spherical radome.
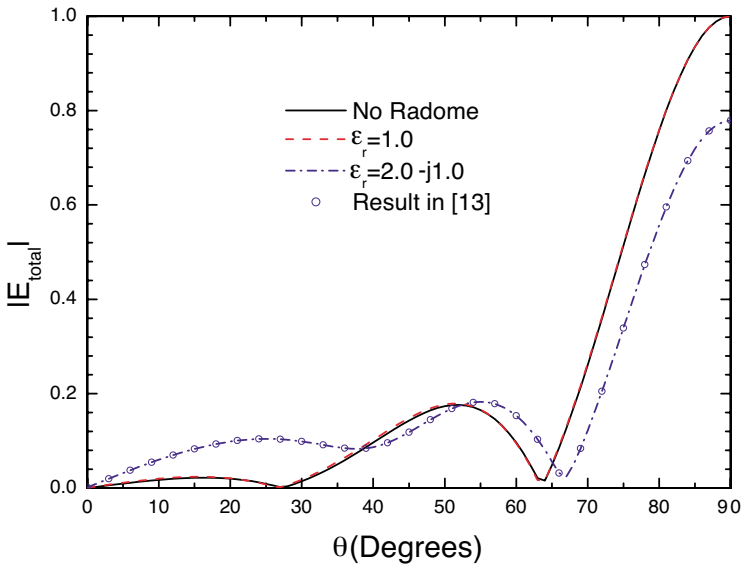
Figure 8. The normalized radiation fields at $r = 100\,\text{m}$ of a dipole array inside a spherical shell.

discretized into 5346 and 6072 triangular patches respectively, leading to totally 34254 unknowns. The radiated fields of the dipole array through the shell at a distance of $r = 100\,\mathrm{m}$ under two cases ($\varepsilon_r = 1.0$ and $\varepsilon_r = 2.0 - j1.0$) are computed and shown in Fig. 8. The radiation of the array in free space is also plotted as reference and all the curves are normalized with respect to the maximum value of the radiated field in free space (appear at $\theta = 90°$). As expected, the radiation of the radome-array system under the case of $\varepsilon_r = 1$ totally agrees with that of the array in free space. Under the case of $\varepsilon_r = 2.0 - j1.0$, the radiated fields are weakened at the directions near $\theta = 90°$ but enhanced at the directions near $\theta = 0°$ due to the presence of the radome. The computed results also agree very well with the exact solution in [13]. For this example, it is estimated that the conventional MoM requires over 8.74 Gbyte memory and will cost 36.8 hours to obtain the final solution on a Pentium 2.4 G PC if enough memory is available. However, the present method requires only 179 Mbyte memory, about 2% that of the conventional MoM and yield an over 73.4% reduction in the CPU time.

4. CONCLUSION

A fast method based on the surface integral equation (SIE) and the precorrected-FFT algorithm is presented for the analysis of antenna radome systems. The problem is formulated using the PMCHW approach for dielectric objects. The integral equations are solved using the method of moments (MoM) and the precorrected-FFT algorithm is used to compute the matrix-vector product in iterations. The application of the P-FFT algorithm significantly reduces the memory requirement and computational cost of the MoM. Therefore, the present method can be applied to analyze radomes of size much larger than that can be handled by the conventional MoM. Several numerical examples were presented, illustrating the accuracy and capability of the method. Radomes of different shapes and parameters are considered. Both the interior fields received inside the radome under a plane wave incidence and the radiated far fields of an elementary dipole inside the radome are investigated. Although for clarity of the description, we only presented the formulations for a single layered dielectric radome, the present method is in fact applicable to any objects consisting of piecewise homogeneous bodies, even composite conducting and dielectric objects.

REFERENCES

1. Gao, X. J. and L. B. Felsen, "Complex ray analysis of beam transmission through two-dimensional radomes," *IEEE Trans. Antennas Propagat.,* Vol. 33, No. 9, 963–975, Sept. 1985.

2. Einziger, P. D. and L. B. Felsen, "Ray analysis of two-dimensional radomes," *IEEE Trans. Antennas Propagat.,* Vol. 31, No. 3, 870–884, March 1983.

3. Orta, R., R. Tascone, and R. Zich, "Performance degradation of dielectric radome covered antennas," *IEEE Trans. Antennas Propagat.,* Vol. 36, No. 11, 1707–1713, Dec. 1988.

4. Wu, D. C. F. and R. C. Rudduck, "Plane wave spectrum-surface integration technique for radome analysis," *IEEE Trans. Antennas Propagat.,* Vol. 22, 497–500, 1974.

5. Hodges, R. E. and R. Samil, "Evaluation of dielectric physical optics in electromagnetic scattering," *AP-S International Symposium (Digest),* Vol. 3, 1742–1745, Ann Arbor, MI, USA, June 1993.

6. Arvas, E., A. Rahhalarabi, U. Pekel, and E. Gundogan, "Electromagnetic transmission through a small radome of arbitrary shape," *IEE Proc.-Microw. Antennas Propag.,* Vol. 137, No. 6, 401–405, Dec. 1990.

7. Arvas, E. and S. Ponnapali, "Scattering cross section of a radome of arbitrary shape," *IEEE Trans. Antennas Propagat.,* Vol. 37, 655–658, May 1989.

8. Gordon, R. K. and R. Mittra, "Finite element analysis of axisymmetric radomes," *IEEE Trans. Antennas Propagat.,* Vol. 41, No. 7, 975–981, July 1993.

9. Yurchenko, V. B., A. Altinas, and A. Nosich, "Numerical optimization of a cylindrical reflector-in-radome antenna system," *IEEE Trans. Antennas Propagat.,* Vol. 47, 668–673, April 1999.

10. Li, L. W., M. S. Leong, P. S. Kooi, T. S. Yeo, and Y. L. Qin, "Radiation of an aperture antenna covered by a spherical-shell chiral radome and fed by a circular waveguide," *IEEE Trans. Antennas Propagat.,* Vol. 46, No. 5, 664–671, May 1998.

11. Li, L. W., M. S. Leong, L. Zhou, T. S. Yeo, and P. S. Kooi, "Improved analysis of antenna radiation from circular aperture covered by a dielectric hemispherical radome shell," *IEE Proc. — Microw. Antennas Propag.,* Vol. 147, No. 2, 144–150, April 2000.

12. Abdel Moneum, M. A., Z. Shen, J. L. Volakis, and O. Graham, "Hybrid PO-MoM analysis of large axis-symmetric radomes," *IEEE Trans. Antennas Propagat.,* Vol. 49, No. 12, 1657–1666,

Dec. 2001.

13. Lu, C. C., "Dielectric radome analysis using multilevel fast multipole algorithm," *2001 AP-S International Symposium and URSI National Radio Science Meeting,* Vol. 4, 730–733, Boston, USA, July 8–13, 2001.

14. Huang, X. J. and Y. W. M. Chia, "The effect of radome on the transmitted electromagnetic field," *1998 AP-S International Symposium and URSI National Radio Science Meeting,* 2194–2197, Atlanta, Georgia, USA, June 21–26, 1998.

15. Rao, S. M., D. R. Wilton, and A. W. Glisson, "Electromagnetic scattering by surfaces of arbitrary shape," *IEEE Trans. Antennas Propagat.,* Vol. 30, No. 3, 409–418, May 1982.

16. Phillips, J. R., "Error and complexity analysis for a collocation-grid-projection plus precorrected-FFT algorithm for solving potential integral equations with Laplace or Helmholtz kernels," *Proc. of 1995 Copper Mountain Conference on Multigrid Methods,* April 1995.

17. Phillips, J. R. and J. K. White, "A precorrected-FFT method for electrostatic analysis of complicated 3-D structures," *IEEE Trans. Computer-Aided Design of Integrated Circuits and Systems,* 1059–1072, Vol. 16, No. 10, Oct. 1997.

18. Nie, X. C., L. W. Li, N. Yuan, T. S. Yeo, and Y. B. Gan, "Fast analysis of scattering by arbitrarily shaped three-dimensional objects using the precorrected-FFT method," *Microwave and Opt. Techn. Letters,* Vol. 38, No. 1, 30–35, 2002.

19. Nie, X. C., L. W. Li, and N. Yuan, "Precorrected-FFT algorithm for solving combined field integral equations in electromagnetic scattering," *J. of Electromagn. Waves and Appl.,* Vol. 16, 1171–1187, 2002.

20. Yuan, N., T. S. Yeo, X. C. Nie, and L. W. Li, "A fast analysis of scattering and radiation of large microstrip antenna arrays," *IEEE Trans. Antennas Propagat.,* Vol. 51, No. 9, 2218–2226, Sept. 2003.

21. Phillips, J. R., "Error and complexity analysis for a collocation-grid-projection plus precorrected-FFT algorithm for solving potential integral equations with Laplace or Helmholtz kernels," *Proc. of 1995 Copper Mountain Conference on Multigrid Methods,* April 1995.

22. McLaren, A. D., "Optimal numerical integration on a sphere," *Mathematics of Computation,* Vol. 17, 361–383, 1963.

23. Topsakal, E., M. Carr, J. Volakis, and M. Bleszynski, "Galerkin operators in adaptive integral method implementations," *IEE Pro.*

Xiao-chun Nie received the B.Eng., M.Eng. and Ph.D. degrees in Electrical Engineering from Xi'an Jiaotong University, University of Electronic Science and Technology of China and Xidian University in 1988, 1993, and 2000, respectively. From 1993 to 1997, he was a lecturer in the University of Electronic Science and Technology of China, Chengdu, China. From Sept. 2000 to Aug. 2002, he worked as a Research Fellow in Singapore-MIT Alliance, National University of Singapore. Since Sept., 2002, he joined Temasek Laboratories as a research scientist. His main interests include numerical analysis of scattering, radiation problems, microwave circuits and antennas.

Ning Yuan received the B.Eng. and M.Eng. degrees in Electrical Engineering from University of Electronic Science and Technology of China, Chengdu, China in 1993 and 1996, respectively and the Ph.D. degree in electrical engineering from Xidian University in 1999. From Sept. 1999 to July 2000, she worked as a Postdoctoral-Fellow in Telecommunications and Industrial Physics, CSIRO, Sydney, Australia. From Aug. 2000 to June 2002, she was with the Department of Electrical and Computer Engineering, National University of Singapore, as a Research Fellow. Currently, she is a Research Scientist of Temasek Laboratories, National University of Singapore. Her main interests are in computational electromagnetics.

Le-Wei Li received the B.Sc. degree in Physics from Xuzhou Normal University, Xuzhou, China, in 1984, the M.Eng.Sc. degree in Electrical Engineering from China Research Institute of Radiowave Propagation (CRIRP), Xinxiang, China, in 1987 and the Ph.D. degree in electrical engineering from Monash University, Melbourne, Australia, in 1992. In 1992, he worked at La Trobe University (jointly with Monash University), Melbourne, Australia as a Research Fellow. Since 1992, He has been with the Department of Electrical Engineering at the National University of Singapore where he is currently an Associate Professor. Since 1999, he has been also part-timely with High Performance Computation for Engineered Systems (HPCES) Programme of Singapore-MIT Alliance (SMA) as a SMA Fellow. His current research interests include electromagnetic theory, radio wave propagation and scattering in various media, microwave propagation and scattering in tropical environment, and analysis and design of antennas.

Tat-Soon Yeo received the B.Eng. (with honours) and M.Eng. degrees from the National University of Singapore, in 1979 and 1981, respectively, and the Ph.D. degree from the University of Canterbury, New Zealand, in 1985. Since 1985, he has been with the Electrical Engineering Department, National University of Singapore, where he is currently a Professor. His current research interests are in wave propagation and scattering, antennas, and numerical techniques.

Yeow-Beng Gan received the M.Eng. and B.Eng. (Hons) degrees in electrical engineering from the National University of Singapore, in 1994 and 1989, respectively. He has been with the DSO National Laboratories (formerly the Defence Science Organization) since 1989. He was the founding member of the antenna group in DSO, and was responsible for building up the technical capabilities in the area of antenna analysis and design. He became a Principal Member of Technical Staff in 1998. In May 2001, he was seconded to the Temasek Laboratories, National University of Singapore, where he is currently a Principal Research Scientist. His research interests include periodic arrays for antennas and radomes, wave physics, computational electromagnetics, and modeling of composite materials. He is a Senior Member of IEEE.